



Universiteit
Leiden
The Netherlands

Granular flows : fluidization and anisotropy

Wortel, G.H.

Citation

Wortel, G. H. (2014, November 19). *Granular flows : fluidization and anisotropy*. *Casimir PhD Series*. Retrieved from <https://hdl.handle.net/1887/29750>

Version: Not Applicable (or Unknown)

License: [Leiden University Non-exclusive license](#)

Downloaded from: <https://hdl.handle.net/1887/29750>

Note: To cite this publication please use the final published version (if applicable).

Cover Page



Universiteit Leiden



The handle <http://hdl.handle.net/1887/29750> holds various files of this Leiden University dissertation

Author: Wortel, Geert

Title: Granular flows : fluidization and anisotropy

Issue Date: 2015-11-19

THE ROLE OF ANISOTROPY IN GRANULAR FLOW

5.1 Introduction

In this chapter we study the influence of the anisotropy of a granular packing on its flow and rheology. When a granular system is sheared, the particles rearrange and form a dilated, anisotropic packing [47, 117–124]. We believe that the buildup and release of anisotropy influences many granular experiments, typically during transients and reversals. In this chapter we will develop a method to measure the anisotropy *explicitly*.

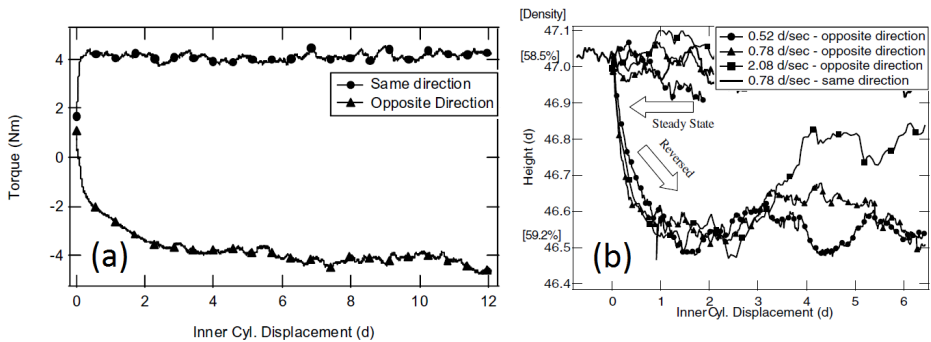


FIGURE 5.1: (a) Torque as a function of strain for a flow reversal experiment. When a fully disordered packing is first sheared, is it isotropic and the required T is low. After a strain of about a grain diameter, the steady state T is reached. When reversing the flow direction (bottom curve), the required T initially is very low. (b) The height and density of the packing. Upon reversal, the packing compacts. Image from [117].

An example where the anisotropy plays a role is an experiment by the group of W. Losert, where the flow of a granular material is investigated in a Taylor-Couette geometry [117]. The emphasis of this work is the response of the flow to a reversal of the flow direction. Two main figures from the paper are shown in Fig. 5.1. In (a), the torque that is required to shear the system, is plotted as function of the strain. Initially, there is a short transient where, for very low strain, the torque is very low. After this stage, when a steady state anisotropy and density have been reached, the system is in a steady state and $T \approx 4$ Nm. When the flow is reversed, there is a new transient where, initially, T is very low and the packing compacts (b). After a transient in the strain of around 5 particle diameters, a new steady state is reached. This experiment shows the influence of the anisotropy of the packing: both the rigidity and the density of the packing change when the shear is reversed. Similar results are also found in a frictionless system [118].

In general, the anisotropy of the packing resists shear. This can also be seen in the force chains that are formed in the direction *counter* to the flow [118, 119]. This is visualized in Fig. 5.2, which is made using photo elastic disks [118]. In the figure, the white arrow indicates the flow direction; the white lines through the particles are the visualization of the force chains.

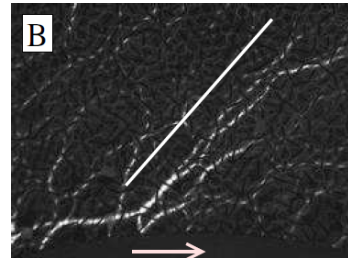


FIGURE 5.2: Using photo elastic disks, the force chains, directed opposite to the flow, can be visualized [118].

In a third example, the rheological curve $T(\Omega)$ of a granular material is measured in the split-bottom geometry [47]. At the bottom of the container there is a rotating disk which fluidizes the system [38] (main flow). Higher up in the system, the flow curves are measured via the rotation of a vane (secondary flow) connected to a rheometer for different rates of the bottom disk. It is found that, in the absence of any main flow, the probe experiences a clear yield stress, whereas for any finite flow rate, the yield stress disappears and the secondary rheology takes on the form of a double exponential relation between Ω and T . This secondary rheology does not only depend on the magnitude of T ,

but is anisotropic – which is shown by varying the relative orientation of the probe and main flow [47].

We perform our experiments of the anisotropy with the setup that was introduced in Sec. 2.2. The basic idea is as follows: we prepare a system by shearing it in rate control until we reach a steady, critical state [125], with a certain constant torque and anisotropy. When we then just vibrate this packing, the vibrations will relax the anisotropy, which leads to a small rotation of the disk in the direction counter to the direction of the initial shear. We measure this rotation with the rheometer, where a larger rotation means that the packing was more anisotropic. This explicit way to measure the anisotropy is a beautiful example of what is possible with our experimental setup that combines shear and vibration.

	Anisotropy	Density
Flow	increase	decrease
Vibrations	decrease	increase

TABLE 5.1: Flow and vibrations compete in terms of both anisotropy and density.

We study the anisotropy as a function of flow rate Ω and vibration intensity Γ . Whereas the flow *builds* anisotropy, the vibrations *relax* the packing. This means that there is a competition between the two, which will eventually lead to a equilibrated value of the anisotropy. Interestingly, this is very similar to density, which is increased by vibrations [126] and decreased by flow [18]. The situation is summarized in Table 5.1. When interpreting the data it is important to be aware of the subtle relation between shear and vibrations and the possible influence of density changes.

5.2 Protocol

The protocol that we use to measure the anisotropy is shown schematically in Fig. 5.3. When *building* the anisotropy, we impose a flow rate Ω_{shear} and vibration intensity Γ_{shear} . When *probing* the anisotropy we impose $T = 0$ and Γ_{probe} , where the rotation of the disk is purely caused by the relaxation of the anisotropic packing. The protocol is complex, which originates from the fact that we cannot instantly change from building the anisotropy to measuring it. If we were to abruptly change from finite Ω to $T = 0$, the inertia of the disk would cause it to keep rotating, which

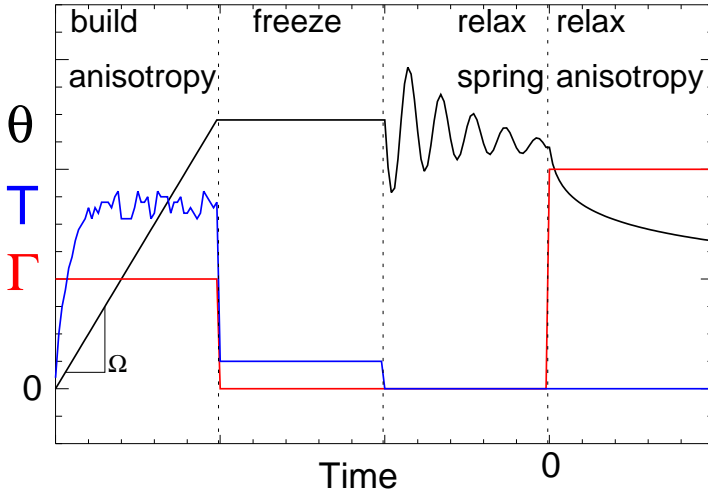


FIGURE 5.3: A schematic representation of the measurement protocol.

would interfere with measuring the relaxation. In addition, the spring, that forms the flexure between the disk and the rheometer, is stretched during the stage when we build the anisotropy. When switching to $T = 0$, the spring relaxes, which results in a significant oscillation on the signal. To circumvent these two complications, the following protocol is developed:

Preshear (not shown in figure): We start with a preshear that consists of 5 s shear at 1 rps, followed by 10 s shear with -1 rps and again 5 s at 1 rps. We conclude with a waiting period of 10 s during which the system is not sheared. During the entire preshear stage, the vibrations are already switched on at value Γ_{shear} .

Stage 1: This is the stage during which we build the anisotropy into the system. There are two control parameters: the vibration intensity Γ_{shear} and the constant rotation rate Ω_{shear} . We verify that we reach steady state flow by measuring T and making sure that it equilibrates. At the slowest Ω_{shear} that we probe, this takes approximately 1.6×10^4 s.

Stage 2: Since we want the disk to be stationary at the beginning of the measurement of the relaxation, we impose $\Omega = 0$. To freeze the anisotropy,

we simultaneously switch to $\Gamma = 0$. The system is now frozen, with the anisotropy still present in the packing.

Stage 3: Now that the disk is frozen and the rheometer is at $\Omega = 0$, the flexure is still stretched. We therefore switch to $T = 0$ while $\Gamma = 0$. The flexure now relaxes without significantly influencing the frozen packing.

Stage 4: We switch on the vibration (this moment is defined $t = 0$ s) and measure the relaxation of the system. We probe at $\Gamma_{\text{probe}} = 0.4$ and a sample rate of 5 Hz for 28 s. Since the flexure is relaxed and the rheometer axis can rotate freely, there is no difference between the deflection of the axis above and below the flexure (we have verified this with the optical encoder that measures the position below the disk that we introduced in Sec. 4.2). This means we can measure the relaxation using the rheometer.

We perform five measurements for each combination of Γ_{shear} and Ω_{shear} (except for the $\Omega < 10^{-5}$ rps, where we measure three times), and average the results thus obtained.

5.3 Steady State Relaxation

5.3.1 Relaxation Speed

We measure the relaxation for $\Gamma_{\text{shear}} = 0, 0.2, 0.4, 0.5, 0.6, 0.7, 0.8$ and $\Omega = 1, 0.316, 0.1, \dots, 10^{-6}$ rps, at $H/R_s = 0.33$ and $\Gamma_{\text{probe}} = 0.4$. In Fig. 5.4(a) we present the raw relaxation curves $\theta(t)$, where the color represents the relaxation speed at $t=0$ s. The relaxation speeds vary over a large range, but for all data, the relaxation becomes slower over time. Apart from some exceptions, the curves do not intersect.

To see how the relaxation varies with Ω_{shear} and Γ_{shear} , we want to extract a number for the relaxation speed from the $\theta(t)$ -curve using a fit. From the data in Fig. 5.4(a), we see that the relaxation curves seem to have a logarithmic shape (this cannot be true for all t , since $\log(t) \rightarrow \infty$ for $t \rightarrow \infty$, whereas our data does not). We find that we cannot fit the data using a 1-parameter fit. The reason for this is that not only the overall relaxation speed, but also the curvature of $\theta(t)$ varies per data set. To take into account both properties of the relaxation curve, we fit the data with:

$$\theta(t) = a \cdot \log\left(\frac{t+b}{b}\right), \quad (5.1)$$

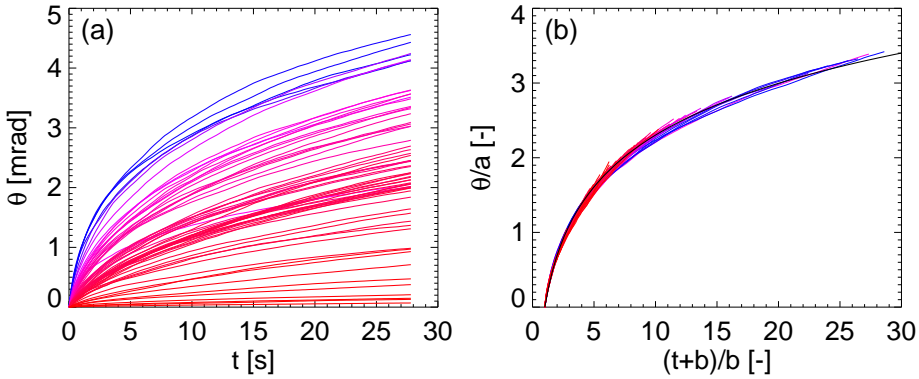


FIGURE 5.4: (a) The raw $\theta(t)$ relaxation curves. The color represents the relaxation speed at $t=0$ s. (b) A collapse of the data onto the master curve $\log[(t+b)/b]$ (plotted in black) using Eq. 5.1.

where b is a measure for the curvature (a *higher* b corresponds to *less* curvature), and a/b is the slope of the relaxation curve at $t = 0$. In addition, the fit function is chosen such that $\theta = 0$ at $t = 0$. In Fig. 5.4(b), we show that the fit with Eq. 5.1 works well by using it to collapse the data onto the master curve $\log[(t+b)/b]$.

To test if we could fit the data with a 1-parameter fit function, we plot the correlation between the initial slope $R = a/b$ and the curvature b in Fig. 5.5(a). We see a correlation where, in general, a faster initial relaxation corresponds to a more curved relaxation curve. However, the relation is quite scattered, which means that a 1-parameter fit would correspond significantly less to the data.

To investigate the quality of the fits, we calculate their standard weighted χ^2 [127] and show the results in Fig. 5.5(b). It can be seen that the logarithmic fit matches the data better for fast relaxations. This is also visible in the collapse of the raw data in Fig. 5.4(b). Here, the slow (red) relaxation curves do not collapse perfectly, but lay just above the master curve for large t . We find that, for low R , the initial relaxation is relatively fast, but for $t > 5$ s, the curvature is very low (an example is plotted in Fig. 5.10(a)). This results in a shape that does not fully match a logarithm.

Hence, the scatter in Fig. 5.5(a) suggests that it is hard to characterize the relaxation curve with a single parameter, and the correlation in

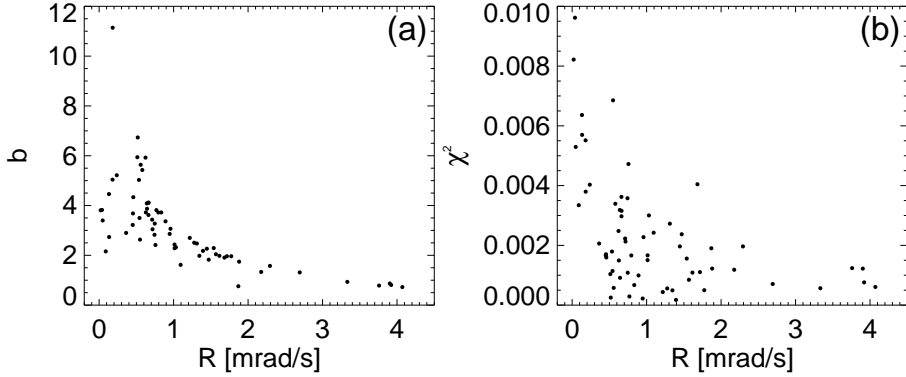


FIGURE 5.5: (a) A scatter plot of the initial relaxation rate $R = a/b$ versus the inverse curvature b . There is a clear correlation, however, for low R , the scatter is large. (b) A scatter plot of the quality of the fit χ^2 vs R . There is a trend that the fit is better for faster relaxations.

Fig. 5.5(b) shows that the fit with Eq. 5.1 systematically works better for fast relaxations. However, we already know that the relaxation curves cannot be true logarithms as our data does not go to $\theta = \infty$. Moreover, as shown by the relatively low values of χ^2 and the good collapse in Fig. 5.4(b), the fits do match the data closely. Fig. 5.4 shows that the general shape of the relaxation curves is robust, and the curves do not intersect. Therefore, we are confident that we can characterize the relaxation process by the single parameter R - defined as the initial relaxation speed at $t = 0$, a/b - as it is a good proxy for the anisotropy of the frozen state. We have verified that the main results that we report are independent of the precise choice of order parameter.

5.3.2 Dependence on (Ω, Γ) and (T, Γ)

In Fig. 5.6(a) we show R as function of the control parameters Γ and Ω . The red curve corresponds to the case without vibrations, $\Gamma = 0$. We see that, for this curve, R is essentially independent of Ω . This is what we expect: at $\Gamma = 0$, the flow is rate independent for the range in Ω that we measure (except for $\Omega > 0.1$ rps). As a result, different values of Ω correspond to the same anisotropy and R ; it will only take a different amount of time to reach the steady state. For $\Omega > 0.1$ rps, R decreases. We be-

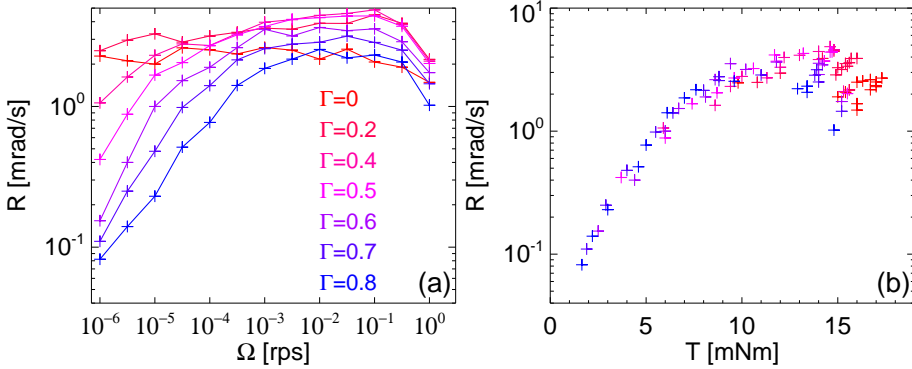


FIGURE 5.6: (a) The relaxation R as a function of the control parameters Γ and Ω . (b) The data collapses when we plot R as a function of the steady state T that we measure during stage 1 where we build the anisotropy.

lieve this is caused by the flow itself, which is so fast, that it fluidizes and relaxes the packing. Overall, the values of R for $\Gamma = 0$ seem surprisingly low, we will discuss this in Sec. 5.5.1.

For $\Gamma > 0$, the situation is more complex. During stage 1, there is a competition between the flow, that is increasing the anisotropy, while the vibrations are relaxing it. For low Ω , this results in a monotonic lowering of R with Γ . Surprisingly, for intermediate $\Omega \approx 10^{-2}$ rps, R is non-monotonic in Γ —the relaxation is strongest for $\Gamma \approx 0.4$. This means that, even though the system is relaxing during stage 1, R for $\Gamma = 0.4$ is larger than for $\Gamma = 0$. This suggests that more anisotropy can be built into a weakly vibrated and thus softened packing. There is, however, a second effect that could play a role in our system; density. Contrary to the anisotropy, flow decreases the density [18], while vibrations increase it [126]. From our current data it is hard to determine whether the stronger relaxation is caused by the anisotropy or by the density.

To see how the relaxation is related to T , we plot R as a function of the steady state T and Γ during stage 1 in Fig. 5.6(b). In this representation, we find a nice data collapse, especially for the slow flows. When Γ is increased, the flow rate will be higher for equal T , but because of the higher vibrations, the anisotropy also relaxes more. The collapse indicates that, in terms of relaxation, these two effects cancel. In other words: it

is the T that sets how much anisotropy is built into the system, or even: it is the anisotropy that determines how much T is required for the flow. The concept that a stress-dependent back stress is generated in sheared granular materials, is also known from geophysical kinematic hardening models [128].

The data collapse in Fig. 5.6(b) also implies that when trying to understand granular flow and searching for a constitutive relation [68–70, 90], the anisotropy is a relevant factor that should be taken into account.

5.3.3 Conclusion

In this section we studied how anisotropic a packing becomes after shearing at certain Ω and Γ . After a certain strain, a steady state is reached where the effects of shear (that builds anisotropy) and vibrations (that release it) balance. We can then measure the anisotropy by probing how fast the packing relaxes (R) as we impose $T = 0$ while vibrating.

We find that for $\Gamma = 0$, R is constant. For $\Gamma > 0$, as expected, R decreases with decreasing Ω . Surprisingly, for $\Omega \approx 0.01$ rps, R is non-monotonic in Γ . This suggests that R could be determined by two physical properties of the system, likely the anisotropy and the density.

5.4 Dynamics of Anisotropy

In the previous section we studied the relaxation of sheared packings that were in *steady state*; here we will investigate how the anisotropy builds up by measuring the relaxation of packings that are in a *transient* state.

We focus on two questions. First, we probe whether the anisotropy has a unique steady state, by studying its evolution from state 1 to state 2, varying state 1. Second, we investigate how the relaxation curves $\theta(t)$ evolve during the transient between two steady states.

We begin by discussing the transient to a steady state from the pre-sheared state in Sec. 5.4.1. In Sec. 5.4.2 we discuss the results of experiments with an extended protocol, involving two different stages whose Γ , Ω , and duration we vary independently.

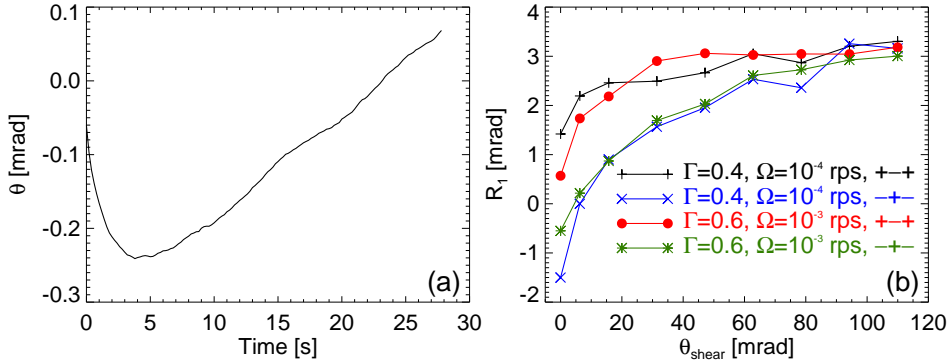


FIGURE 5.7: (a) Complex relaxation curve where different parts of the system have opposite anisotropy. This situation occurs when the last stage of the preshear is opposite to the flow during the evolution stage. (b) The dependence of R_1 on the strain during the evolution stage.

5.4.1 Relaxing from Preshear to Steady State

The packing that we create with the preshear protocol is well-defined and reproducible, but already anisotropic. This implies that during the evolution stage of the protocol of Fig. 5.3 (stage 1), the anisotropy evolves from an already anisotropic state. Because of the large range of shear rates $\dot{\gamma}$ that are present in split-bottom flow, the local transient time scale can be expected to vary with location, and the global relaxation time is not easily guessed. Moreover, the relative direction of preshear and evolution stage matters. If the last stage of the preshear was in the counterclockwise (–) direction, and the evolution stage is in the clockwise (+) direction, during the transient, different parts of the packing will have opposite anisotropies. An example of the complex, non-monotonic relaxation curves that result from this is shown in Fig. 5.7(a), where we believe that at different times, different locations in the system dominate the relaxation process. Of course, a complex relation curve such as in Fig. 5.7(a) cannot be fitted with Eq. 5.1. Therefore, we use the alternative R_1 to characterize the relaxation, which is defined as the angle that the disk rotates back during the first 28 s.

To probe the duration of the transient, we determine the plateau where R_1 does no longer depend on the amount of shear during the evolution

stage θ_{shear} . In Fig. 5.7(b) we investigate this for $\Gamma = 0.4$, $\Omega = 10^{-4}$ rps and $\Gamma = 0.6$, $\Omega = 10^{-3}$ rps. The preshear always consists of three phases, but we vary in which direction the last phase is. We can either start in the (+) direction, then do (-) and end in (+) (in Fig. 5.7(b) we label this as $+++$), or the opposite ($-+-$). The evolution stage is always performed in the (+) direction. The data in Fig. 5.7(b) shows that, for the $-+-$ preshears, R_1 is negative for small θ_{shear} , which indicates that the overall anisotropy is dominated by the preshear. For $\theta_{\text{shear}} \gtrsim 100$ mrad, R_1 takes a constant value, independent of whether the preshear was $+++$ or $-+-$. This shows that the steady state anisotropy has been reached, and that the corresponding value of R_1 is independent of the direction of preshear. We note that all steady state data in Sec. 5.3 was taken for $\theta_{\text{shear}} \geq 100$ mrad. The final stage of the preshear, at the fast rate of 1 rps, has been imposed for a large strain of 3×10^5 mrad.

5.4.2 Two Stage Relaxation

In the experiments that were described in Sec. 5.3 and 5.4.1, relaxation from fast preshear to steady flow was studied. To probe how the material's internal structure evolves with time, we now extend the experimental protocol such that it contains two consecutive evolution stages during which we shear the system at fixed Γ_i and Ω_i . In this extended protocol there are two transients, first from the preshear to stage 1 (with reversal), then from stage 1 to stage 2 (without reversal). Since we are interested in the time evolution of the anisotropy, the strain in each stage (measured in terms of the angle θ_i) is a crucial control parameter. This results in a total of six control parameters for the experiment: Ω_1 , Γ_1 and θ_1 during stage 1, and Ω_2 , Γ_2 , θ_2 during stage 2. The precise protocol is shown in Fig. 5.8.

We will address several questions using the two stage relaxation. First, by varying the flow in stage 1, we will probe whether the anisotropy of stage 2 is unique. Second, we will examine how the relaxation curve evolves during the transient in between steady states.

Results – In Fig. 5.9 we show the main results of the experiments, all for $H/R_s = 0.6$ and $\Gamma_{\text{probe}} = 0.8$. As in the previous section, we measure each relaxation five times and report the average, where the error bars represent the standard deviation over the five runs. We note that, once the relaxation has been measured, it is impossible to restart the flow and simply

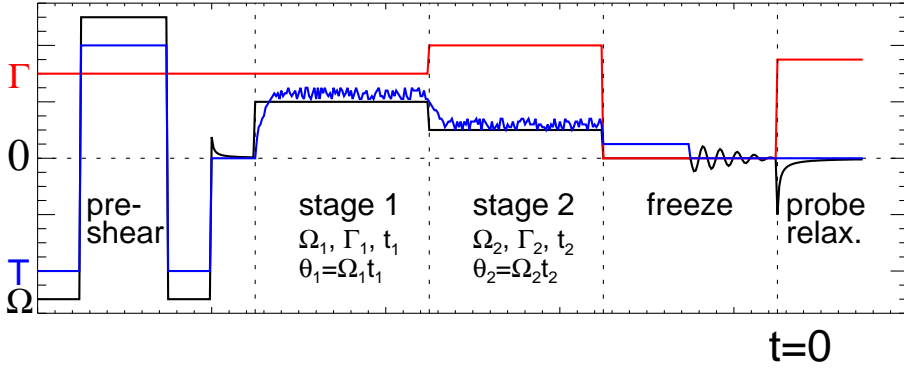


FIGURE 5.8: The extended protocol where there are two evolution stages after the pre-shear. There are two transients, one from the preshear to the first stage, the other from the first to the second stage. The parameters that characterize a stage are Ω_i , Γ_i , and the total disk rotation θ_i .

measure the next data point. Therefore, for each measurement, we have to start from the beginning (with the preshear). As a consequence, the measurements performed with the extended protocol are relatively time consuming. Also note that for small θ_1 , complex relaxation curves such as in Fig. 5.7(a) occur, so that we cannot fit all our data with Eq. 5.1. As the temporal resolution of our data is too low to find the instantaneous relaxation rate using a numerical derivative, we will characterize the relaxation curves by R_1 ; the angle that the disk rotates back during the first 28 s.

In Fig. 5.9(a-b) we show experiments for $\Gamma = 0.7$, where the black data corresponds to $\Omega_1 = 10^{-2}$ rps and $\Omega_2 = 10^{-4}$ rps, and the red data to the opposite, *i.e.* $\Omega_1 = 10^{-4}$ rps and $\Omega_2 = 10^{-2}$ rps (in Fig. 5.9, all the left panels correspond to stage 1, and the right panels to stage 2). In Fig. 5.9(a) the black data shows that for $\Omega_1 = 10^{-2}$ rps, the anisotropy monotonically reaches a plateau value of $R_1 \approx 8$ mrad. If we then change to the second stage with $\Omega_2 = 10^{-4}$ rps (panel (b), black), we see that the relaxation monotonically drops to a steady state value of $R_1 \approx 4$ mrad. This trend is consistent with the prior results: for lower Ω , the vibrations are relatively more important, which leads to a less anisotropic packing.

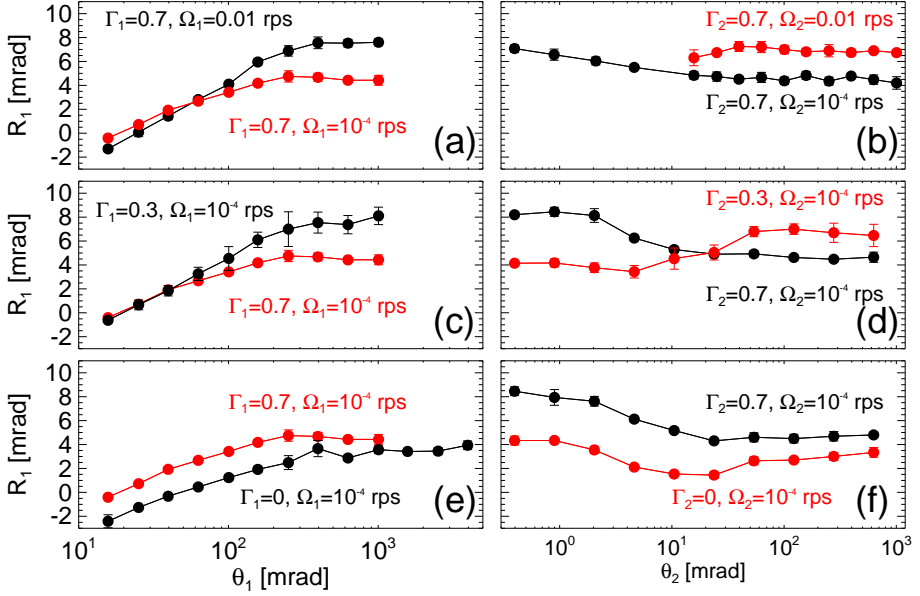


FIGURE 5.9: The relaxation R_1 for experiments using the extended protocol as shown in Fig. 5.8. By interchanging the Γ or Ω that is imposed during stage 1 and stage 2, we can investigate the uniqueness of the steady state values of the anisotropy.

In red, we show the inverse experiment. In Fig. 5.9(a) we find that the red data ($\Omega_1 = 10^{-4}$ rps) equilibrates at $R_1 \approx 4$ mrad, and for $\Omega_2 = 10^{-2}$ rps, the red data in Fig. 5.9(b) evolves to $R_1 \approx 8$ mrad. Hence, for these parameters, the asymptotic value of R_1 only depends on its current stage and not on the previous stage; irrespective of the system's history, at $\Gamma = 0.7$, an Ω of 10^{-4} rps corresponds to a R_1 of 4 mrad, and $\Omega = 0.01$ to $R_1 \approx 8$ mrad. We finally note that (with the exceptions for small θ_1), all the relaxations are logarithmic, and the anisotropy changes monotonically.

In (c-d) we keep Ω constant at 10^{-4} rps, but change Γ between 0.3 and 0.7. Also here the steady state is history-independent and unique, and the anisotropy evolves monotonically.

In Fig. 5.9(e-f) we illustrate qualitatively different curves that govern the evolution between $\Gamma = 0.7$ and $\Gamma = 0$. Several saillant features stand out. First: for $\Gamma_1 = 0$, the transient seems longer than in previous data, but after a strain $\theta_1 \approx 500$ mrad, the system reaches a steady state $R_1 =$

4 mrad. Second: the steady state R_1 is the same for $\Gamma_1 = 0.7$ and $\Gamma_1 = 0$ – this is consistent with the observation in Fig. 5.6(a) that at intermediate flow rates, the anisotropy is non-monotonic in Γ . Third: comparing the steady state values in (e) and (f), we find that they are consistent: also here, the steady state value of R_1 is unique. Fourth: the behavior of the black curve in (f) is surprising: if we switch on the vibrations, the relaxation almost instantly *increases* from $R_1 \approx 4$ mrad to $R_1 \approx 8$ mrad. A possible explanation for this is that the vibrations compact the packing, and that a denser packing leads to a higher anisotropy. With increasing θ_2 , the packing adapts to its steady state $R_1 \approx 4$ mrad. Fifth: as shown by the red curve in (f), the evolution from $R_1 \approx 4$ mrad (which is the steady state for $\Gamma = 0.7$) to the similar relaxation value $R_1 \approx 4$ mrad for $\Gamma = 0$, is strongly non-monotonic: R_1 does not remain constant at 4 mrad, but dips to 1 mrad (while T peaks to a maximum) before growing back to 4 mrad. This means that for small strains, the flow first *removes* anisotropy from the packing. This suggests that even though $\Gamma = 0.7$ and $\Gamma = 0$ correspond to the same amount of relaxation, the way the anisotropy is built into the packing is different between these two cases.

The examples in (e-f) suggest that $\Gamma = 0$ is a special case. Even though the steady state values of the anisotropy are unique, the evolutions show surprising non-monotonic behavior, indicating that there are different ways for the packing to be anisotropic.

We proceed by looking at the raw relaxation curves to see how they change as the system evolves towards a new steady state. In Fig. 5.10 we show the curves that correspond to the red data in Fig. 5.9(f) for $\theta_2 = 0.40, 24, 628$ mrad – as indicated in the legend. The black and red curves correspond to similar R_1 , however, the black curves (as emphasized by the normalized curves in (b)) are slightly more curved. This is consistent with Fig. 5.5(a) where we found scatter in the relation between the initial slope and the curvature of the relaxation curve.

The blue curves in Fig. 5.10(a) correspond to the dip in Fig. 5.9(f). For these curves, the relaxation is significantly slower than for the red and the black data. This demonstrates that even though it is impossible to grasp all the precise characteristics of the curve with a single parameter, the dip in Fig. 5.9(f) is a robust effect which would also have been easily picked up by the original parameter R .

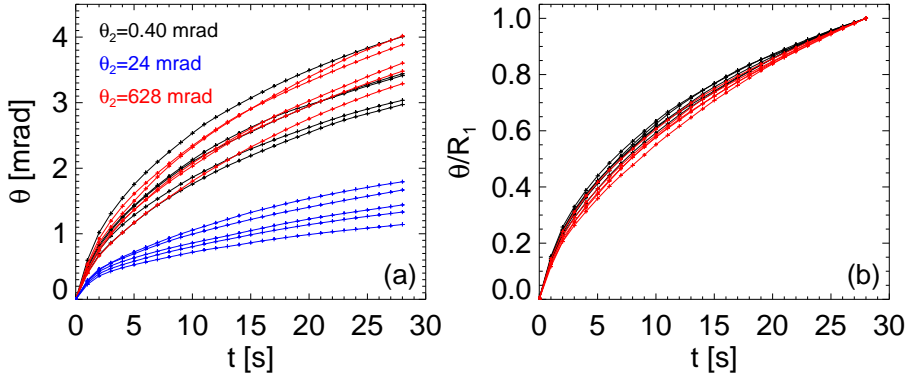


FIGURE 5.10: (a) The relaxation curves for the red data points in Fig. 5.9(f) with θ_2 [mrad] = 0.40, 24, 628. The black and the red curves correspond to similar R_1 , however, the black data is slightly more curved. The relaxation in the blue data is significantly slower. (b) The red and black data as in (a), normalized by R_1 , confirm that the black data is more curved.

During the evolution between stage 1 and 2, the relaxation curves appear to be logarithmic – just as for steady states. As a check, we calculate χ^2 for the fits and compare the values to the ones found for the steady state relaxation in Fig. 5.5(b). We find that the values are consistent, suggesting that the shape of the relaxation curves during the evolution is the same as the shape for steady state relaxations.

Finally, we want to verify the *robustness* of the deviating behavior for $\Gamma = 0$ that was observed in Fig. 5.9(e-f). Therefore, we perform more experiments, with different Ω_1 , Γ_1 , Ω_2 , and Γ_2 (either Γ_1 or Γ_2 is 0), and show the results in Fig. 5.11. As we are only interested in the surprising behavior during stage 2, we take a constant θ_1 of 600 mrad (long enough to reach a steady state), and probe only the relaxation during the second stage.

The blue and the green curve in Fig. 5.11 represent the case where $\Gamma_1 = 0$ and $\Omega_1 = 10^{-4}$ rps. As we know from Fig. 5.9, the corresponding $R_1 = 4$ mrad. The behavior for these cases is the same as for the black curve in Fig. 5.9(f); as soon as the vibrations are switched on, the anisotropy suddenly increases significantly. The fact that the increase is of different

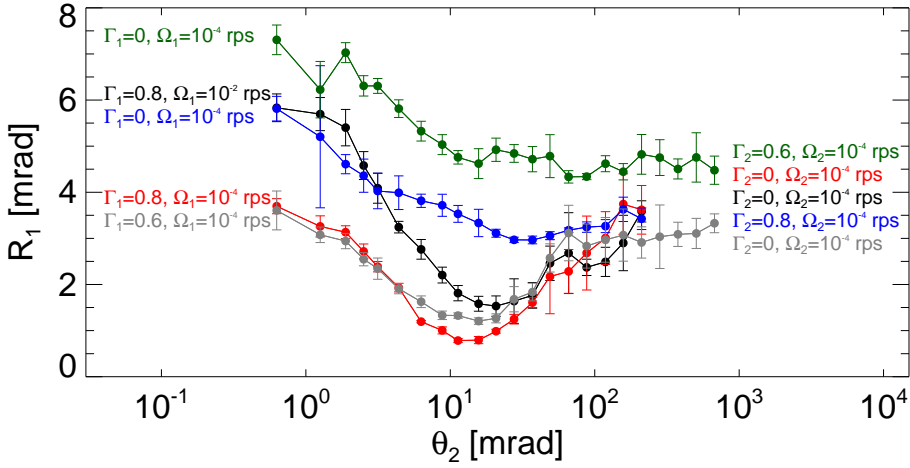


FIGURE 5.11: Additional experiments to investigate the deviating results when either Γ_1 or Γ_2 is 0. In this case, we only probe the relaxation during stage 2.

size between the green (which goes to $\Gamma_2 = 0.6$) and the blue curve ($\Gamma_2 = 0.8$), shows that the increase is Γ -dependent.

The red and the gray curve are for the case where $\Gamma_2 = 0$. Again, we see the characteristic significant dip in R_1 , similar to the dip in the red curve in Fig. 5.9(f).

For the black curve we change both Γ and Ω . We start from a very anisotropic packing that we reached with relatively fast flow: $\Gamma_1 = 0.8$ and $\Omega_1 = 0.01$ rps. We then switch to slow flow (10^{-4} rps) at $\Gamma_2 = 0$, and again see a strongly non-monotonic $R_1(\theta_2)$.

Hence, all the curves in Fig. 5.11 are consistent with the behavior that was observed in Fig. 5.9.

5.5 Conclusion and Discussion

In this chapter we have investigated the anisotropy of packings by probing how the anisotropy relaxes from the packing as it is weakly vibrated. In Fig. 5.6(b) we found that the strength of the relaxation is set by the torque that was imposed during the flow. This observation suggests that the an-

isotropy is a crucial ingredient towards finding a constitutive relation for granular flows.

In Fig. 5.9 we found that for each Γ , Ω , there is a unique value of the anisotropy – independent of the history of the system. The relaxation curves, both for a steady state and an evolving packing, can be fitted using a two-parameter logarithmic function. There is a robust trend that this fit matches the data slightly better for faster relaxations.

From our measurements it is hard to precisely quantify the anisotropy at a certain point in time. First, the non-monotonic evolution of the anisotropy in time in Fig. 5.9 and Fig. 5.11 shows that the relaxation is a complex quantity, which seems to depend not only on anisotropy, but also on density. We expect these two effects to be coupled [129], so it requires great care to separate the influences of the two and to assign a value to the anisotropy. A second difficulty is the complex flow profile in the split-bottom geometry. We find that, because of the large range of strain rates that are present in the system, different parts of the system can correspond to a different value of the anisotropy. The relaxation that we measure is a collective result of the relaxation of all the different regions. In Fig. 5.9(a,c,e) it seems that the building of anisotropy from the presheared state is logarithmic in time. However, because of spatial inhomogeneities, we cannot claim that this dependence is true for all, especially more simple, flow geometries. In fact, in simulations it is found that anisotropy grows exponentially in time [130]. Another consequence of the complex shape of the relaxation curves is that they cannot precisely be characterized using a single parameter. However, the relaxation curves are similar in size enough to allow us to obtain robust results, independent of the precise order parameter.

In general, we expected flow to *build* anisotropy and vibrations to *relax* it. In Fig. 5.6(a) this was confirmed for finite Γ and small Ω , which corresponds to a significantly slower relaxation. For intermediate flow rates, $\Omega \approx 0.01$ rps, the relaxation is non-monotonic in Γ – also suggesting that the relaxation that we measure is the result of at least two different physical properties of the system. This physical picture is backed up by the data in Fig. 5.9 and Fig. 5.11. In these results we found the additional evidence that equal relaxation does not imply that the precise anisotropic state of the packing is also the same. Even though the steady state values of the relaxation are unique and independent of the system’s history,

we observed surprising behavior during the (non-monotonic) evolutions, where in some cases vibrations *increase* the relaxation and flow *decreases* it. All the deviating transients involve $\Gamma = 0$, either as initial or destination state. This shows once more that the granular flow in a system with “zero temperature” differs significantly from the case with weak vibrations.

5.5.1 Outlook

For future experiments, we suggest two modifications to the protocol that was introduced in Fig. 5.3.

First, the way we switch off the shaker during the freezing stage can be improved. For the experiments reported in this chapter, we stopped the shaking abruptly – at an arbitrary phase of the oscillation. However, this can result in a fast relaxation of the shaker to its equilibrium position, which might affect the packing. We have performed exploratory measurements where we smoothly damp out the vibrations using a Doepfer A-143-2 voltage controlled amplifier that gradually decreases the wave amplitude to 0 over a period of ten oscillations. We found that the main results reported in this chapter, including the torque collapse in Fig. 5.6(b), are unaffected by this modification of the protocol.

Second, we would modify the way the flexure is relaxed during the freezing stage. In the reported experiments, we abruptly switch to $T = 0$, which we do not expect to alter the frozen packing. However, at $\Gamma = 0$, the flexure is stretched with a torque of the order of the yield torque, and we cannot be certain that the impact, that the packings endures when we switch to $T = 0$, does not affect the packing. In fact, this impact could explain the surprisingly low values of R for $\Gamma = 0$ in Fig. 5.6. To improve the protocol, the torque can be reduced to zero smoothly. We stress that the main result of this chapter, the torque collapse in Fig. 5.6(b), is not sensitive to the way the torque is reduced, as the collapse occurs for low torque experiments, where the torque in the spring is significantly below the yielding torque of the frozen packing.